SANDIA NATIONAL LABORATORIES
SOLAR THERMOCHEMICAL HYDROGEN PRODUCTION (STCH) PROGRAM

QUARTERLY PROGRESS REPORT FOR JULY 1, 2013–SEPTEMBER 30, 2013

SUBMITTED BY: TONY MARTINO, (505) 844-0652, MARTINO@SANDIA.GOV

RECIPIENT: SANDIA NATIONAL LABORATORIES

PRINCIPAL INVESTIGATORS: TONY MCDANIEL (925) 294-1440, AMCDANI@SANDIA.GOV
ALAN WEIMER, (303) 492-3759, ALAN.WEIMER@COLORADO.EDU

PROJECT TEAM: IVAN ERMANOSKI, (505) 284-0740, IERMANO@SANDIA.GOV
NATHAN SIEGEL, (570) 577-3827, NATE.SIEGEL@BUCKNELL.EDU
JIANHUA TONG,(303) 273-3053, JIANTONG@MINES.EDU

CONTENTS

Sandia National Laboratories

Sandia National Laboratories is a multi-program laboratory managed and operated by Sandia Corporation, a wholly owned subsidiary of Lockheed Martin Corporation, for the U.S. Department of Energy's National Nuclear Security Administration under contract DE-AC04-94AL85000.

FY 2013 MILESTONES/DELIVERABLES

The shaded milestones represent activities that will be conducted if an over-budget request of $200K to Sandia is granted.

Task/Milestone Description	Status	Comp.	Plan
Solar Thermochemical Hydrogen Production (STCH)			
Subtask 1.1: Metal Oxide Cycle Studies at Sandia National Laboratories			
Materials Discovery and Characterization			
Develop guiding principles for perovskite modification via site substitution based on documented trends of oxidation enthalpy, reduction entropy, and various other material properties reported in the literature for a small class of perovskites. A metric for success will be the discovery of one or more key indicators that show a positive correlation towards increasing the redox capacity, lowering reduction temperature, or improving kinetics.	Ongoing. Three methodologies have been devised based on thermodynamic quantities (reduction enthalpy, reduction entropy, and oxidation enthalpy), as well as perovskite structure theory. Experimental measurements are currently underway to validate and refine the design principles.	30%	2/13
Synthesize at least 50 different perovskite compounds. These materials will be identified by application of the "guiding principles" established in the previous task. Material synthesis to be conducted in collaboration with Colorado School of Mines (CSM). A metric of success will be to synthesize 500 mg each of phase-pure materials.	Synthesized between 200–1,000 mg sized samples of 45 different perovskite compounds from 9 elements (Al, Cr, Ce, Fe, La, O, Sr, Ti, Zr). Most compounds showed expected crystallographic phases: either cubic, orthorhombic, or hexagonal lattice structures. Most compounds were also found to be single phase (i.e., little to no impurity content).	100%	6/13

Task/Milestone Description	Status	Comp.	Plan
Characterize the thermodynamic and kinetic performance of synthesized perovskites using Sandia's rapid thermal-cycling stagnation flow reactor and thermo-gravimetric analysis available at both Sandia and CSM. A metric for success will be the discovery of a perovskite formulation that can split water, thermally reduce at a temperature less than 1,350 ºC, and has twice the capacity of undoped ceria (> 100 µmoles H_2/g).	Reported in Q1FY13 the discovery of Sr- and Mn-doped $LaAlO_3$ (SLMA) that outperforms CeO_2. SLMA reduces at T < 1350 ºC and produces > 300 µmoles H_2/g (better than 9 times more than CeO_2 when reduced at 1,350 ºC). In Q2FY13, we characterized kinetics for Fe-doped calcium titanate ($CaTi_{1-x}Fe_xO_3$) and found water-splitting (WS) activity similar to CeO_2. This is the first demonstration of a perovskite formulated from earth-abundant ores that can split water (i.e., produce H_2), though no real performance gains relative to CeO_2 were evident. In Q4FY13 we characterized the thermodynamic behavior of three SLMA compounds over a range of O_2 partial pressure and temperatures relevant to STCH conditions. We are in the process of constructing a defect model for this material and using the experimental result to model reactor behavior.	100%	9/13
Reactor Development			
Material conveying performance will be measured using the existing engineering test stand, under ambient conditions of temperature and pressure. Metrics of success are the ability to convey material at 8 g/s in the 3-inch auger and 30 g/s in the 8-inch auger.	Particle transport assessed using a 3-inch auger designed for heat recuperation (narrow finned, double helix). The 3-inch auger transports 8 g/s at 4 RPM, and 40 g/s at 20 RPM. Achieved particle conveyance rates that exceed reactor design requirement. Postponed the 8-inch test.	100%	9/13
Upgrade the engineering test stand for vacuum-compatible operation up to 200 °C. A preliminary design for a vacuum-capable prototype operating up to 900 °C will be completed.	In progress. Designed and in the process of construction of the vacuum compatible engineering test stand. We expect to be conducting room-temperature vacuum tests by Q1FY14.	65%	9/13
Characterize engineering test stand under conditions of vacuum (10 Pa < p < 10 kPa), gas flow, and increased temperature (T < 200 °C). Metrics of success are the ability to convey material at 30 g/s in the entire design range. The results of these tests will be used to finalize the 900 °C prototype design.	Construction stage.	0%	9/13

Task/Milestone Description	Status	Comp.	Plan
System Analysis			
Develop system-level designs and analyses of central-receiver-based platforms that include additional detail related to the balance of system components for a particle reactor-based hydrogen production system having an annual average solar-to-hydrogen efficiency in excess of 20% (as opposed to 14% in FY12).	Estimated the cooling requirements for the beam-down optic reflector using a heat transfer model. Cooling the secondary can be accomplished via forced air or water cooling methods.	100%	7/13
Assess the cost of hydrogen production from a particle reactor using the H2A3 tool on either a parabolic dish or central receiver platform, to include sensitivity studies showing how system costs can be impacted by technology improvement of major subsystem costs, e.g., heliostats.	Completed multiple iterations of the H2A3 analysis for a dish-based production facility. Continuing to refine the analysis in collaboration with SA, Inc. The cost for hydrogen in the year 2020 is estimated to be \$8.56/kg H_2 based on a conventional material like ceria operating at an STH conversion ratio of 16.6%. The cost is projected to be near the ultimate DOE target of \$2/kg H_2 for an advanced material operating in an advanced SRR at an STH conversion ratio of 34.3%.	100%	9/13
Standardized Screening Method			
Retrofit the stagnation flow reactor to operate at pressure > 1,500 Torr and water concentration ≤ 85 volume %.	5 months after authorization.		
Design and implement a material characterization protocol that adheres to the principles of “best practice.” A flow chart describing key characterization methods to facilitate materials development will be derived and vetted. At a minimum, the flow chart will include benchmarks and recommendations for assessing kinetics, redox capacity, limiting reduction temperature, and cycle durability.	8 months after authorization.		

Task/Milestone Description	Status	Comp.	Plan
Subtask 1.2: ALD Active Thin Films/Support Materials for Ferrite/Hercynite Thermochemical Redox Cycle/Solar Reactor			
Hercynite Redox Nanostructured Materials and Isothermal Cycling			
Synthesize a cobalt ferrite/alumina hercynite active material by atomic layer deposition (ALD) using polymer templates. Demonstrate isothermal redox water-splitting in a stagnation flow reactor at a temperature of 1,350 ºC yielding a H_2 production per gram of total mass of active material greater than 100 µmoles/g.	Demonstrated March, 2013. Isothermal redox carried out at 1,350 ^{o}C produced 217.3 µmole H_2/g active material for 50% steam concentration at a total pressure of 760 Torr.	100%	9/13
Theoretical studies using density functional theory (DFT) will be used to develop an understanding of the isothermal redox cycling process. Evaluate design and efficiency trade-offs between isothermal and conventional temperature-variant thermochemical redox cycle operation using hercynite.	DFT has shown that Fe has the lowest activation barrier for cation migration through the lattice of the spinel, followed by Co, then followed by Ni. Isothermal redox thermodynamics has been developed based on chemical potential has been published.	100%	6/13
Multi-Tube Solar Receiver			
On-sun demonstration at NREL HFSF of cobalt ferrite/alumina hercynite cycle active materials using polymer templates. Demonstrate isothermal redox water-splitting yielding a H_2 production per gram of total mass of active material greater than 100 µmoles/g.	Synthesized materials for the on-sun test. Experiments carried out at NREL in September, 2013, but time on the HFSF ran out as others were scheduled to run. We anticipate completing these experiments by the end of the year	80%	9/13
A model of the tubular reactor will be developed in FLUENT and used to simulate reactor performance. We will evaluate the impact on efficiency of isothermal redox cycling vs. conventional thermochemical redox. A 4.5-kW multi-tube solar reactor will be designed along with a designed solar flux for a predicted dynamic efficiency of greater than 5%.	A dynamic model has been developed and simulations are completed for evaluating isothermal redox vs. conventional temperature-swing redox for the “hercynite cycle” materials contained in an absorbing cavity solar reactor. Preliminary efficiencies greater than 5% have been calculated for a 4.5-kW receiver.	100%	9/13

SUBTASK 1.1: METAL OXIDE CYCLE STUDIES AT SANDIA NATIONAL LABORATORIES

BACKGROUND

The conversion of solar radiation into a chemical fuel such as hydrogen is an engineering challenge; however, unlike solar-derived electricity or heat, it is easier and more efficient to transport and store hydrogen. This point is important because energy demand is rarely matched to incident solar radiation, either spatially or temporally. Two-step solar-driven thermochemical processes based on non-volatile metal oxide cycles are an attractive technology for producing hydrogen from water because of the potential to operate at high solar-to-chemical conversion efficiency with moderate operational demands on land and water resources. Conceptually, solar energy is collected and concentrated using heliostats. This can be accomplished on small scales with trough- and dish-type receivers operating at tens of kilowatts, to large-scale central receivers operating at tens of megawatts. Incident solar radiation can thus be converted to high-temperature process heat and then used to drive a thermochemical water-splitting reaction.

OBJECTIVE

The overall objective of this subtask is to develop a practical solar-driven hydrogen production system based on a non-volatile metal oxide cycle using a particulate media. This process involves the development of a high-temperature particle conveying and reactor system, making improvements to the reactant materials, expanding our understanding of the underlying material thermodynamics and kinetics, updating system performance calculations, and developing economics models.

MATERIALS DISCOVERY AND CHARACTERIZATION

Point of Contact: Tony McDaniel

PROJECT STATUS

In Q4FY13 we conducted a detailed thermodynamic screening of the Sr- and Mn-doped $LaAlO_3$ (SLMA) perovskites discovered this Fiscal Year. This information is necessary to model the expected behavior of this advanced material in Sandia's particle reactor. We also synthesized and screened another novel material formulation that crystallizes in the form of the fergusonite structure. Finally, we re-evaluated the "hercynite" redox cycle chemistry in an effort to better understand the kinetics and mechanisms involved in the water splitting reaction. We will discuss the status of these three activities separately.

Perovskite thermodynamics

The perovskite oxides of $Sr_{0.6}La_{0.4}Mn_{0.6}Al_{0.4}O_3$ (SLMA6464), $Sr_{0.4}La_{0.6}Mn_{0.4}Al_{0.6}O_3$ (SLMA4646), and $Sr_{0.4}La_{0.6}Mn_{0.6}Al_{0.4}O_3$ (SLMA4664) are excellent materials for thermochemical water-splitting. In order to calculate the expected STH conversion efficiency of these materials in the Sandia particle reactor, we need to know the detailed relationship between temperature, oxygen partial pressure, and oxygen nonstoichiometry of the material.

SLMA powders were synthesized by a conventional wet-chemical EDTA acid and citric acid combined complexation method. After processing and calcining, XRD patterns indicated that high purity samples for each of the three SLMA formulations were made. 20 mg of each material was placed into a Setaram System Evolution TGA-DTA/DSC instrument, which was used to measure the change in mass for the SLMA powders at various oxygen partial pressures and temperatures. Figure 1 shows a typical TGA cycle at an oxygen partial pressure of 2×10^{-3} atm. The sample was pretreated to 700 °C and held for 1h in 100 ml/min air, which established the reference state. After evacuating the system and cooling to 300 °C, 100 ml/min 1% O_2 (N_2 balance) was switched on and the thermal gravimetric program started. The mass change was subsequently monitored as the temperature was increased from 300 to 1400 °C, taking 100 °C steps after 800 °C, soaking for 0.5 h at each temperature.

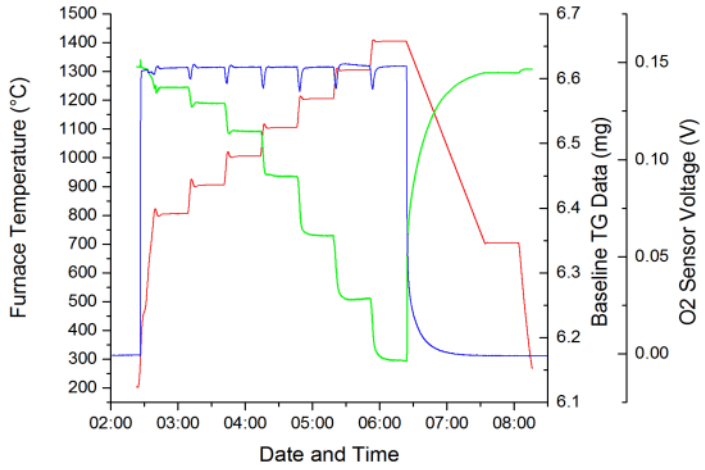

Figure 1. Representative example of a TGA experiment. Temperature profile (red), mass change (green), and oxygen partial (blue) are shown by colored curves, respectively.

The data in Figure 1 can be converted into a log-log plot that represents the extent of oxygen nonstoichiometry (δ) in the material as a function of temperature as illustrated in Figure 2. Here, each oxygen partial pressure condition (vertical row of points) is derived from a single TGA experiment. A simple fit to this data set allows us to extrapolate the thermodynamic behavior of the SLMA compounds to very low oxygen partial pressure. In the event that this does not

provide a sufficiently robust representation to the thermodynamic behavior at low oxygen partial pressure, we will have to collect additional TGA data and then fit this to a more comprehensive oxygen defect model. The example here illustrates the difficulty of obtaining the necessary thermodynamic information for new materials. Conducting experiments at low oxygen partial pressure (< 10^{-8} atm) is quite challenging, and spanning a large oxygen partial pressure range is very time consuming.

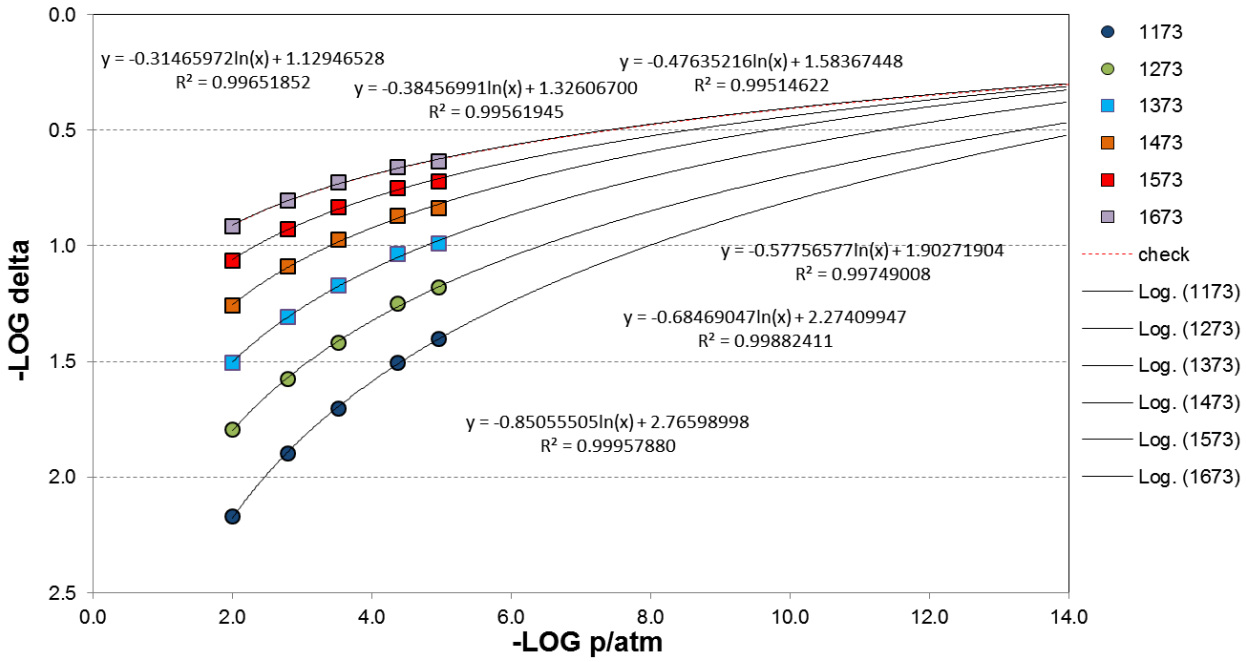

Figure 2. Thermal reduction model for SLMA6464. Symbols are data points, solid lines are individual data fits, and the dashed red line is a universal model for the entire range.

Furgusonite materials

It is well known that reducing CeO_2 to an appreciable extent requires high temperatures, for example the oxygen nonstoichiometry (δ) is only 0.07 at 1500 °C in 10^{-5} atm of O_2. This complication has more to do with the fluorite crystal structure then with the $Ce^{3+/4+}$ redox process itself. Therefore, we sought to incorporate the $Ce^{3+/4+}$redox couple into a different crystal structure in an attempt to discover a new STCH material. Our target structure is fergusonite, specifically a $YNbO_4$ composition where Ce can occupy 100% of the Y sites. We replaced Y with Ce and doped Zr on the Nb site to test a hypothesis that this material will facilitate the $Ce^{3+/4+}$redox process.

$CeNb_{1-x}Zr_xO_4$ (x = 0.0 - 0.15) powders were synthesized by a solid state reaction method. The crystal structure of the as-synthesized powders were characterized by XRD and the diffraction patterns, shown in Figure 3, indicate the tetragonal fergusonite structure formed as opposed to the monoclinic scheelite structure. The results of TGA screening experiments, shown in Figure 4,

indicate that the Zr doped $CeNb_{1-x}Zr_xO_4$ compounds are much easier to reduce than CeO_2 (large δ_{RED} on the x-axis of the plot), and are more easily reoxidized than our SLMA series (points lie above the SLMA compounds on the y-axis of the plot). Based on these observations, we conducted several kinetic screening experiments in the laser-heated stagnation flow reactor and found that the redox kinetics for this material system were exceedingly slow. Given that this material system could have a redox capacity twice that of the SLMA compounds, this chemistry warrants further investigation.

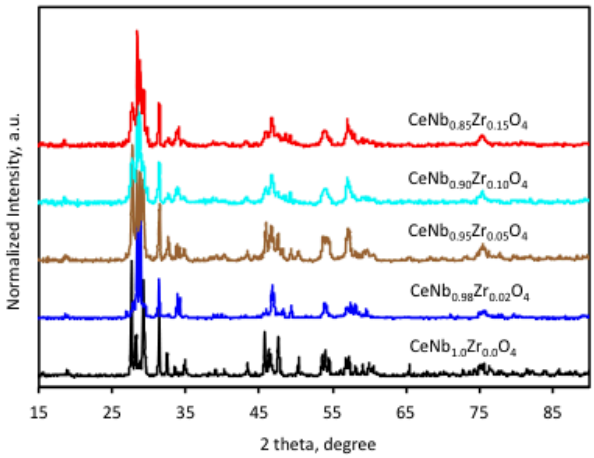

Figure 3. XRD patterns for $CeNb_{1-x}Zr_xO_4$ (x = 0.0 - 0.15) powders calcined at 1500 °C for 24h.

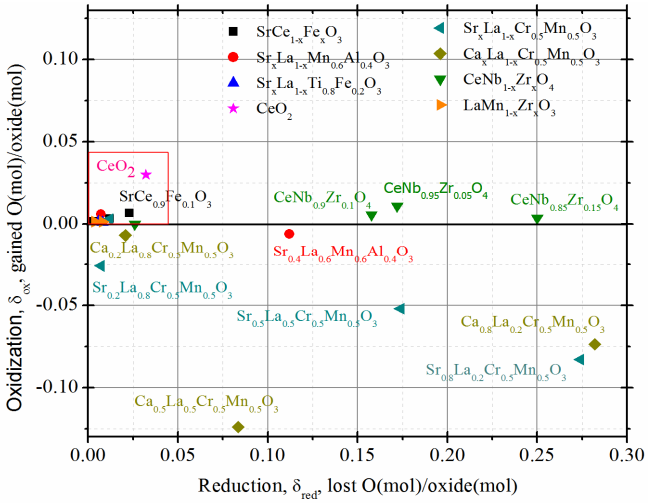

Figure 4. Redox capacity of $CeNb_{1-x}Zr_xO_4$ (x = 0.0-0.15, green inverted triangles) compared with other perovskite oxides.

Hercynite redox mechanism

In Q4FY13 Sandia supported and participated in the re-assessment of the hercynite redox cycle chemistry. As proposed by CU, the water-splitting reaction is a displacement process that occurs according to the following two reactions:

$$CoFe_2O_4 + 3Al_2O_3 \rightarrow CoAl_2O_4 + 2FeAl_2O_4 + 0.5O_2, \quad \text{REDUCTION} \quad (1)$$

$$CoAl_2O_4 + 2FeAl_2O_4 + H_2O \rightarrow CoFe_2O_4 + 3Al_2O_3 + H_2, \quad \text{OXIDATION} \quad (2)$$

Upon thermal reduction (Reaction (1)), a cobalt ferrite spinel reacts with aluminum oxide at high temperature to produce both cobalt and iron aluminate spinels in addition to gas-phase oxygen. Subsequently, when exposed to steam (Reaction (2)) the water-splitting reaction regenerates the original cobalt ferrite spinel and aluminum oxide phases. It has been previously verified that the water-splitting oxidation reaction is kinetically limited at temperatures below 1320 °C and therefore CU has proposed to run this particular redox cycle isothermally at temperatures between 1300 - 1450 °C.

Hercynite's isothermal redox kinetics were measured over a wide range of temperatures and oxidation conditions, the preliminary results of which are summarized in Sub Task 1.2 and will not be repeated here. This body of work is the most comprehensive and well characterized data set for hercynite redox chemistry available to date, and should enable CU to extract an empirical kinetic model sufficiently robust to incorporate into simulations of their multi-tube solar receiver.

Regarding the actual redox mechanism as presented in Reactions (1) and (2), Sandia performed several experiments using in-situ x-ray diffraction (XRD). This instrument is unique in that it allows the measurement of XRD patterns while subjecting the hercynite to the same redox conditions as in the kinetic experiments. That is, at high temperature (1400 °C) and in the presence of either an atmosphere of helium or a mixture of CO_2 in helium. The results of this experiment are shown in Figure 5. In this plot, the in-situ XRD data is shown as a 2-D colored panel with vertical streaks. Overlaid on top of this panel are the powder XRD patterns for the three spinel phases of interest, $CoFe_2O_4$, $CoAl_2O_4$, and $FeAl_2O_4$. Each colored pixel row in the 2-D XRD image is a complete diffraction pattern taken at that particular condition (see legend on right hand side of Figure 5). There are 20 XRD spectra stacked from bottom to top.

Three very pertinent conclusions can be drawn from this data set; (1) a complete absence of the $CoFe_2O_4$ spinel phase during oxidation or reduction, (2) a complete absence of a pure $CoAl_2O_4$ spinel phase during oxidation or reduction, and (3) intensity of the Al_2O_3 diffraction patterns are relatively unchanged. If the bulk hercynite redox chemistry occurred as proposed in Reactions (1) and (2), then there would be streaks at 35.5 2θ ($CoFe_2O_4$) that would disappear in the presence of He (Reaction (1)) and reappear in the presence of CO_2 (Reaction (2)). In addition, the intensity of the Al_2O_3 diffraction peaks would increase and decrease accordingly since the absolute concentration of Al_2O_3 in the bulk presumably changes during the reaction. What is certain is that the "hercynite" cycle is not a displacement reaction. These results indicate the need

for a better understanding of the hercynite redox cycle and have been provided to CU to help inform future research. Our preliminary analysis suggests it is simply a ferrite redox reaction occurring within the hercynite phase trapped inside an Al_2O_3 matrix. Simply put, the chemistry is analogous to well known and well studied ferrite/zirconia composites.

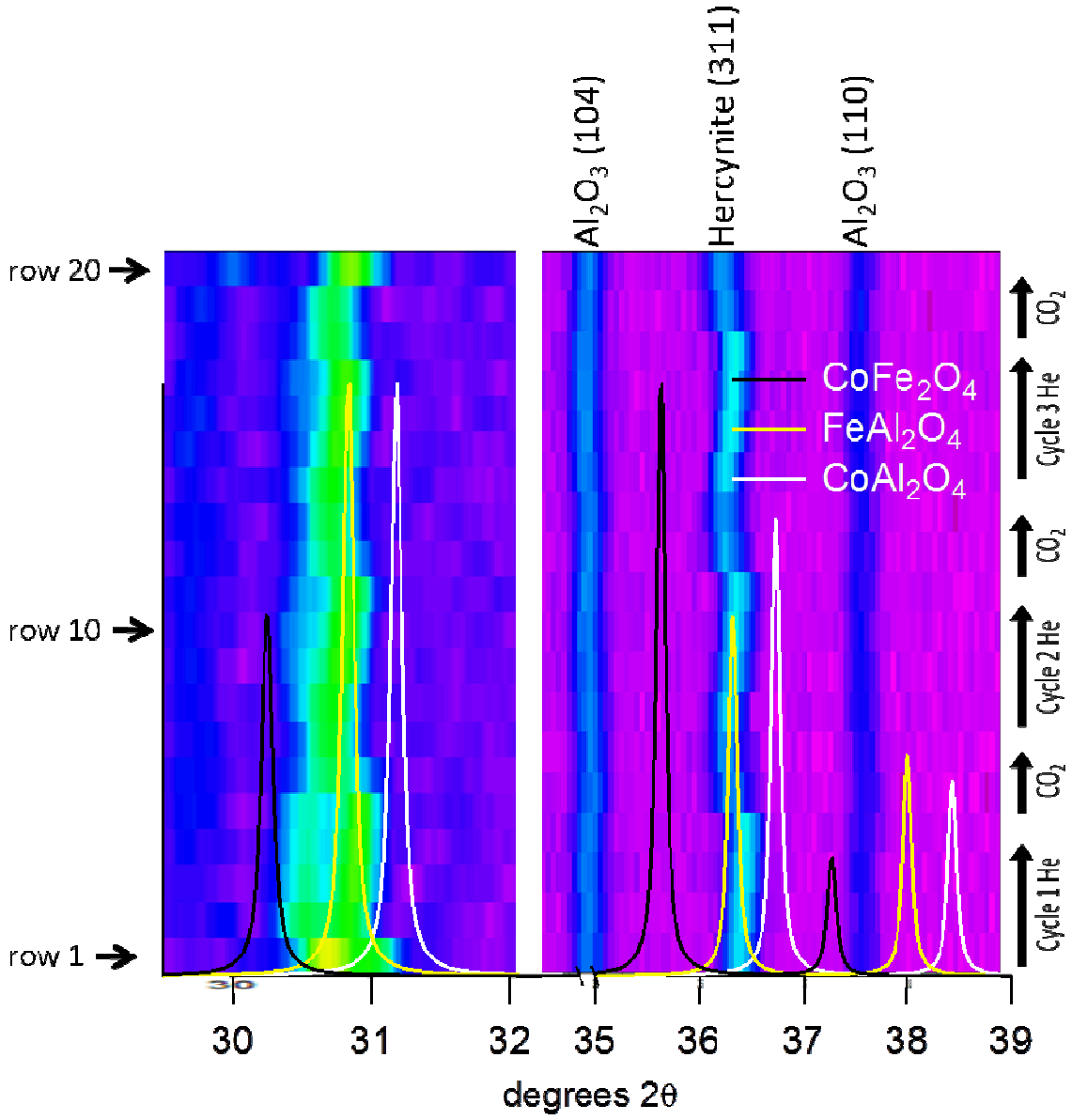

Figure 5. In-situ XRD patterns measured during three successive hercynite isothermal redox cycles taken at 1400 °C. Each pixel row is a complete XRD pattern, 20 patterns are stacked from bottom to top. The right hand legend indicates either exposure to He or CO_2. Diffraction peaks are long vertical streaks in the image.

PLANS FOR NEXT QUARTER AND KEY ISSUES

In Q1FY14 we plan to continue our investigation of other potential STCH material systems, both within and outside of the perovskite crystal structure. We will also develop a robust defect model for the SLMA thermodynamics.

REACTOR DEVELOPMENT

Point of contact: Ivan Ermanoski

PROJECT STATUS

In Q4FY13 the reactor development work focused on two main research areas: (1) reactor modeling, especially as it pertains to *optimal* reactor operating conditions, and (2) design and construction of a vacuum compatible engineering test stand.

In the previous quarter (results reported at the Annual Review and in the Annual Report) we determined the optimal operation temperature difference, $\Delta T=T_{TR}-T_{FP}$, between the thermal reduction and fuel production steps, thus allowing us to map reactor performance more precisely. As noted in this previous work, the gas-gas heat recovery effectiveness was assumed to be $\varepsilon_{GG}=0.95$. It was also shown that for a lower value of ε_{GG}, ΔT_{opt} increases under all conditions. In the current work, we explore the consequences of a reactor design that cannot achieve high heat recovery effectiveness in either the gas (ε_{GG}) or the solid (ε_R). It is known that efficient gas-gas heat recovery at temperatures above 1273 K is an engineering challenge. In fact, we are not aware of any examples of gas-gas heat exchange technology that operates at temperatures near 1773 K. Solid-solid heat recovery under STCH reactor conditions is even more difficult.

The plots presented in Figure 6 illustrate the point. Here the optimal temperature difference, ΔT_{opt}, and resultant *reactor* efficiency (η_R) at this optimum are shown as a function of oxygen partial pressure in the thermal reduction step (p_{TR}) for a range of heat recovery effectiveness factors (ε_{GG} and ε_R). Immediately obvious from the data in these plots is the importance of solid heat recovery; the reactor efficiency decreases by 40% between an ε_R of 0.75 and 0. This result implies that for CeO_2, and negligible solid heat recovery, the theoretical maximum STH conversion ratio (based on the HHV for H_2) is less than 0.13 (assuming 50% collection efficiency). This value is consistent with the scientific literature where published reports are well below 0.05 for the most advanced reactors. The effectiveness of gas-gas heat recovery is similarly dramatic and serves to further illustrate that isothermal operation, challenged by the need for high ε_{GG} at temperatures unachievable in practice (T > 1773 K), is expected to perform at efficiencies much lower than show here. A manuscript detailing our recent findings is in preparation.

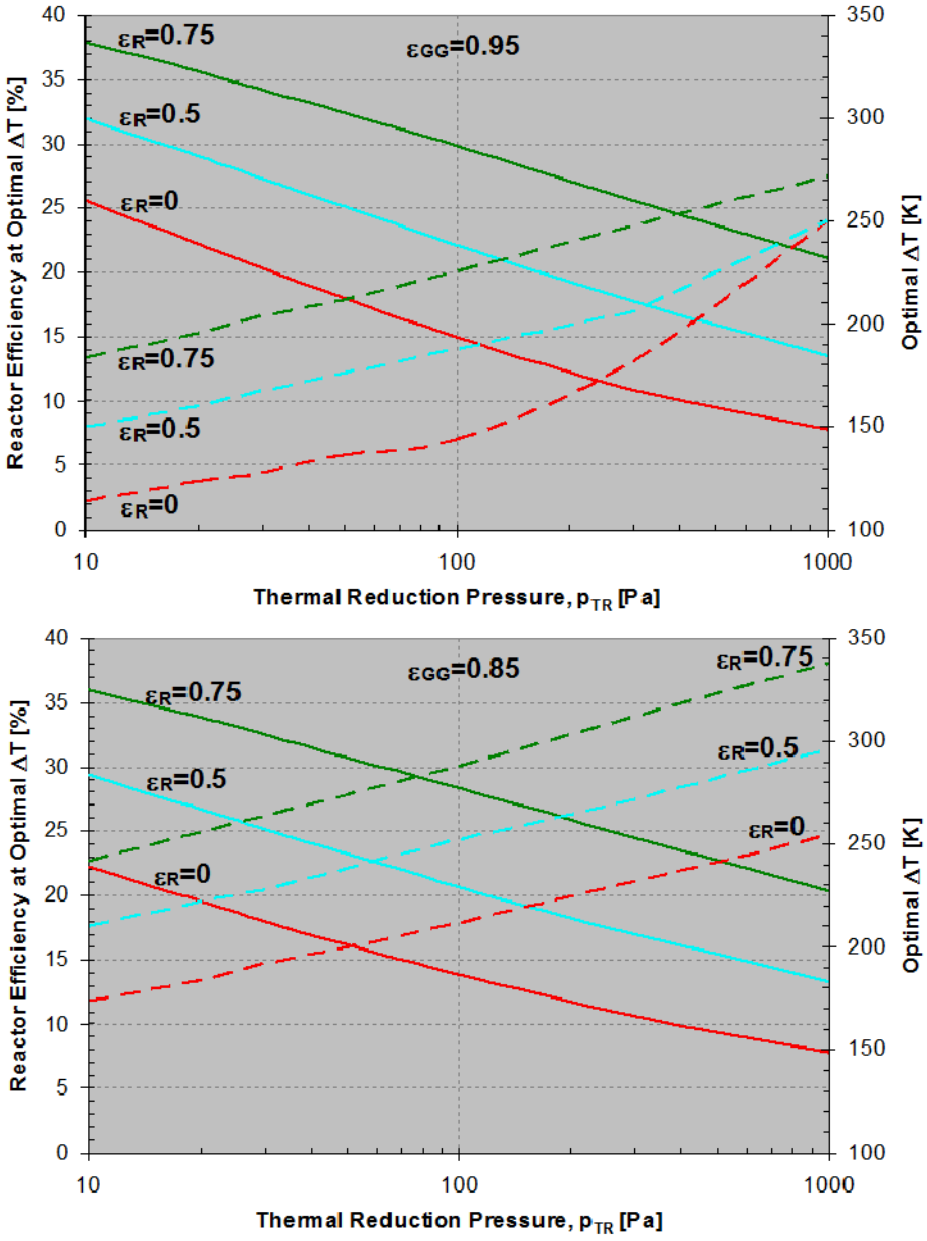

Figure 6. Calculated reactor efficiency (solid lines) and ΔT_{opt} (dashed lines) for three values of ε_R (0. 0.5, and 0.75) and two values of ε_{GG} (0.95 and 0.85).

Most of the necessary custom parts for the vacuum compatible test stand have been delivered, and we proceed with its construction (solid design shown in Figure 7). When completed, we will test particle conveyance in vacuum, pressure separation under realistic pressures and particle flow geometry, and continuous particle flow against a sustained pressure differential. The test stand is also designed modularly so we can add more functionality to it. This includes increasing

the height of the rotary stage and swapping in different design features for high-temperature vacuum operation.

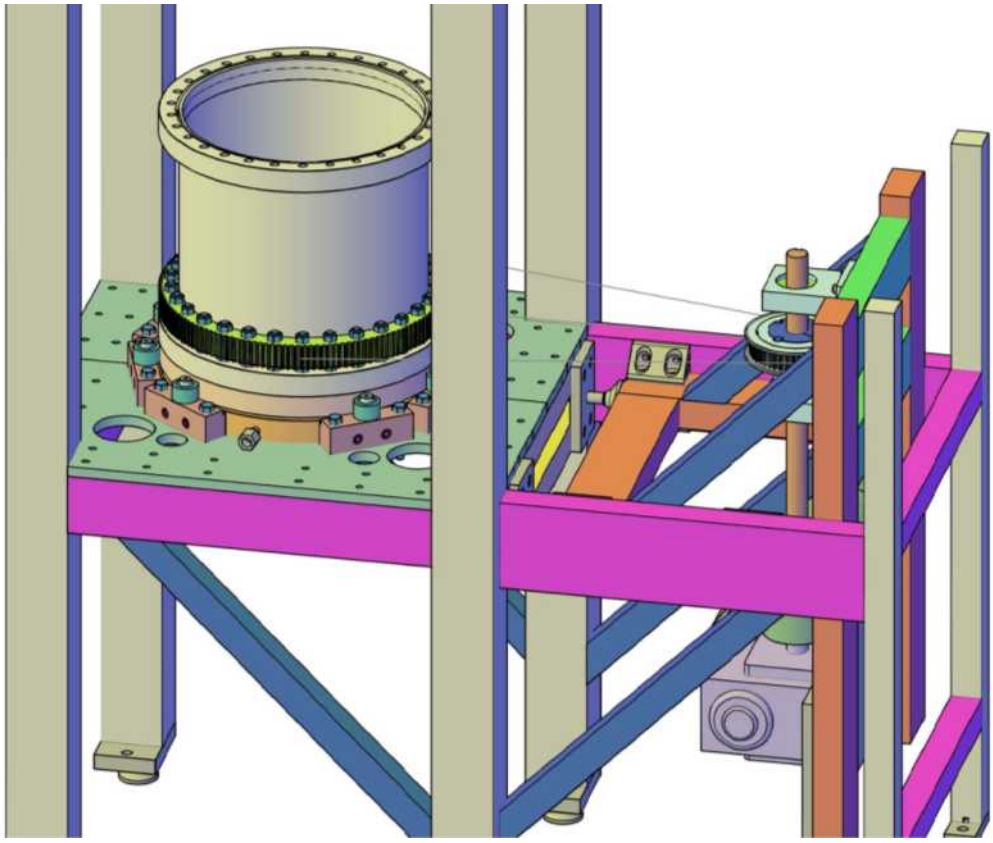

Figure 7. 3-D drawing of vacuum compatible engineering test stand.

PLANS FOR NEXT QUARTER AND KEY ISSUES

In Q1FY2014 we will further pursue reactor modeling, with continued emphasis on establishing the space of optimal operating parameters for ceria and perovskites, as well as increasing the model accuracy. We will also continue construction of the test stand and validate key functionalities as components are integrated into it (vacuum integrity under expected RPM conditions, particle conveying in vacuum, etc.).

SYSTEMS ANALYSIS

Point of contact: Nathan Siegel

PROJECT STATUS

Our first system analysis of a particle reactor operating with a beam-down central receiver was based on the use of cerium oxide as the reactive material and a collection field in which heliostats were located only on the North side of the tower. Recent progress in the development of new reactant materials necessitates a re-evaluation of system level performance to account for the differences between perovskite reactants and cerium oxide with respect to: 1) thermal reduction temperature, 2) oxidation temperature, 3) reaction extent, 4) enthalpy of reaction, and 5) thermal reduction pressure. These parameters influence both the efficiency of the reactor (conversion efficiency) and of the receiver.

In Q4FY13 we performed a field optimization study to determine the collector field layout that yields the highest collection efficiency for a given power level. While the previous analysis was based on a North field configuration, our current optimization strategy also considers a surround field design for the beam down tower. An illustration of the collection system for the beam down tower is shown in Figure 8.

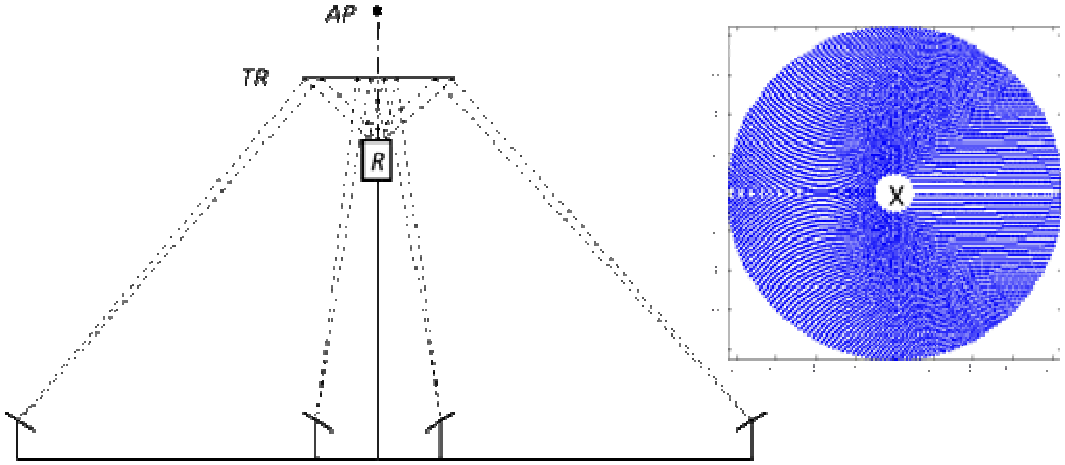

Figure 8. A beam down tower with a with a surround field reflector layout. "AP" denotes the field aim point, "TR" is the tower reflector, and "R" is the reactor. The "X" indicates the location of the tower in each of the field configurations (right).

The parameters that were varied in the field optimization were the outer field radius and angular extent of a North field. The tower height was held constant at 75 m and the inner field radius 10 m. Thirty individual cases (simulations) were used in the optimization. Delsol was used to evaluate the annual field efficiency which includes losses associated with optical reflectivity of all mirrors (, cosine efficiency of the heliostats , blocking and shading , atmospheric attenuation , intercept , and system availability . Additional intercept losses as well as radiative losses from the receiver are calculated separately for each case following aperture sizing. The product of the Delsol-calculated field efficiency and the receiver efficiency is called the collection efficiency, shown mathematically in Equation

1. The receiver efficiency is calculated for each case using the flux distribution calculated by Delsol as an input.

(1)

Annual collection efficiency is the figure of merit used in the evaluation of the different field configurations. This is a function of many parameters including field geometry, geographic location, optical quality of the collectors, and the temperature at which the reactor operates for the endothermic thermal reduction reaction. A summary of the collection efficiency evaluated for a thermal reduction temperature of 1400˚C is shown in Figure 9A, and for a thermal reduction temperature of 1300˚C in Figure 9B.

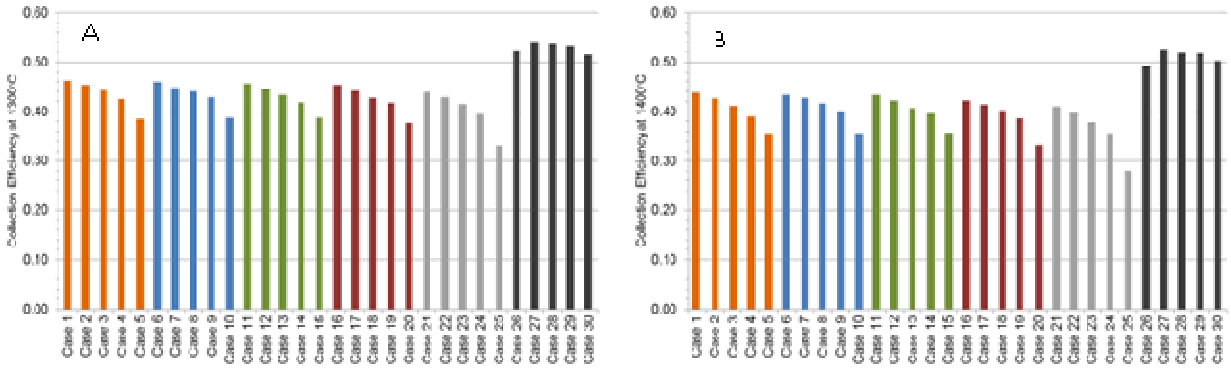

Figure 9. Annual collection efficiency calculated for multiple field configurations using a 75 m tall beam-down central receiver. (A) operation of the thermal reduction reaction at 1300 °C, (B) operation at 1400 °C.

Cases 1-25 in Figure 9 are for a North field configuration (for comparison to the full-field results shown in cases 26-30), and the field size is held constant for each group of colored bars. The angular extent of the field is varied within each group from largest (165˚) to smallest (82.5˚), moving from left to right within each group. The results show that, for any field radius, a larger angular extent will result in greater collection efficiency. This is primarily a result of the fact that the aperture size remains relatively unchanged as the angular extent is varied. Having a larger field, with more heliostats, provides more power to the aperture, increasing the ratio of heat input relative to radiative losses that are essentially fixed by the aperture size and reactor temperature. The effect of field outer radius on collection efficiency is somewhat less pronounced than that of angular extent, with the most efficient North field, Case 1, having an annual collection efficiency of 44%. Temperature does have an impact as well. Case 1 comes in at an efficiency of 46% when operated at 1300˚C due to decreased receiver losses.

Changing the field configuration from a North field to a surround field significantly improves performance (cases 26-30). In a surround field, heliostats are placed all around the tower, allowing much more collector area to be installed for a single tower. As a result, significantly

more energy is provided to the reactor, increasing the average flux across the aperture and improving receiver efficiency relative to a North field. This is essentially the same effect observed when the angular extent of a North field is varied; a surround field has an angular extent of 360°. The peak collection efficiency of 53% is achieved in Case 27, which is a surround field with an outer radius of 115 m and providing 6.3 MW of power to the thermochemical reactor from a total of 9642 heliostats. The power delivered to the reactor is defined as the amount of energy available to the thermochemical reactor after all collection losses have been accounted for. Case 30 is a less efficient configuration, at 50%, but provides nearly 13.5 MW of power to the reactor from a total of 21719 heliostats in a field with an outer diameter of 130 m.

The flux distribution on the flat tower reflector and on the aperture of the reactor is of particular importance for any configuration; the flux level on the aperture is tied to receiver efficiency, while the flux distribution on the tower reflector must be considered when assessing mechanical durability. Figure 10 (A-B) shows the flux distribution for the surround field of Case 27, the most efficient of all field configurations evaluated, at both the tower reflector (A) and at the aperture plane (B). Additional flux maps for Case 30, the highest delivered power of 13.5 MW, are shown for the plane of the tower reflector (C) and the aperture plane (D).

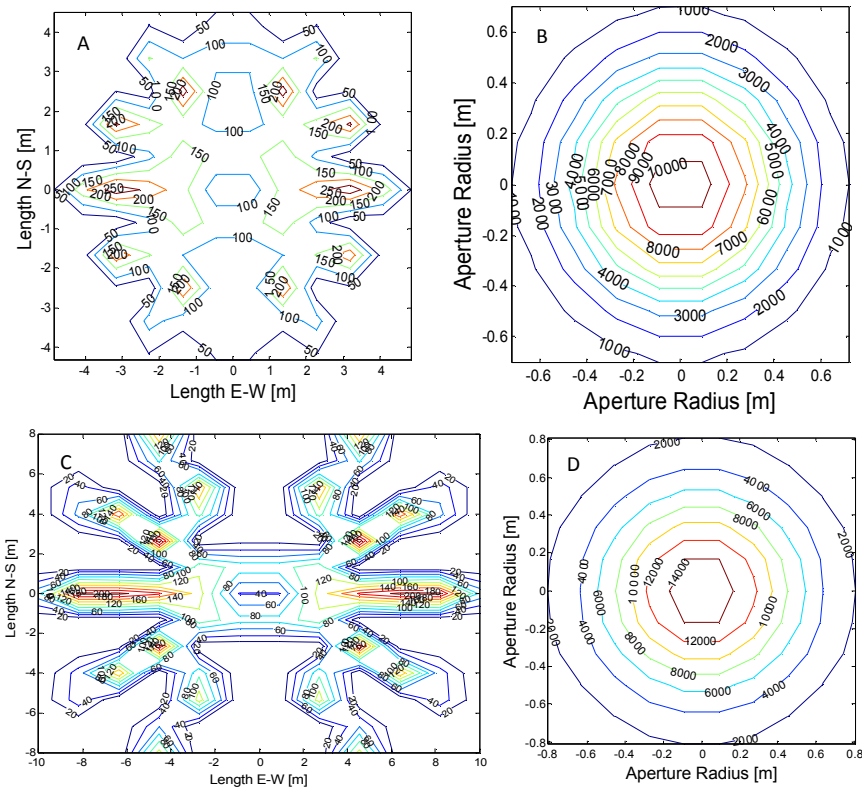

Figure 10. The flux maps for Case 27 at the tower reflector for (A) and aperture (B), and for Case 30 at the tower reflector (C) and aperture (D).

The maximum incident flux level for Case 27 is 282 kW/m^2. This is nearly double that seen in the North field cases. The peak flux on the aperture exceeds 10,000 kW/m^2 with an average of 1551 W/m^2 over the 1.6 m diameter aperture. The resulting receiver efficiency is 85% at 1400 °C. For Case 30, the peak flux on the TR is 214 kW/m^2. The peak flux at the 1.6 m^2 aperture is 15,000 kW/m^2, with an average value of 3261 kW/m^2. The peak flux on the TR is lower for Case 30, despite the larger power level, because the beam down distance is larger (i.e., the tower reflector is more distant from the aperture). While this is good for mirror durability, the size of the TR is rather large; 20 m × 16 m for Case 30 versus 8m × 10 m for Case 27. This illustrates one of the practical limits to the size of an individual tower receiver; as the heliostat field size increases, so does the size of a flat tower reflector for a given tower height. It is possible to move to a curved tower reflector, but that results in poorer optical quality at the aperture because reflected light diverges upon reflection from a curved tower reflector.

PLANS FOR NEXT QUARTER AND KEY ISSUES

The preceding field design and collection system performance data will ultimately be combined with performance predictions for a particle reactor operating with a perovskite reactive material. These predictions will be based on simulations that use, as input, experimentally determined values for key thermodynamic properties including the enthalpy of thermal reduction, reaction extent, the temperature of thermal reduction, and the required oxygen partial pressure during thermal reduction. Preliminary experimental results indicate that the perovskites will exceed the performance of cerium oxide reactants while operating at a considerably lower thermal reduction temperature. In Q1FY14 we plan to implement a finite element based thermal model of the beam down reflector and to design a prototype for experimental evaluation on Bucknell's solar simulator. In addition, we also plan to begin working on the H2A3 analysis for the central receiver configuration of the particle reactor. Finally, we plan to incorporate thermodynamic data for the perovskites into our system level performance model and evaluate the annual efficiency of a particle reactor operating on a small (<10 MW) beam-down power tower.

STANDARDIZED SCREENING METHOD

Point of contact: Tony McDaniel

PROJECT STATUS

No activity; awaiting authorization and additional funding.

PLANS FOR NEXT QUARTER AND KEY ISSUES

No activities planned unless authorization is granted.

PUBLICATIONS/PRESENTATIONS

"Oxide Materials for Thermochemical CO_2 and H_2O-Splitting Using Concentrated Solar Energy", A. Ambrosini, E.N. Coker, M.D. Allendorf, A.H. McDaniel, D. Arifin, E.C. Miller, J. Tong, and J.E. Miller, ASME 7th International Conference on Energy Sustainability, Minneapolis, MN, USA, 14-19 July, 2013.

"The Intrinsic Oxidation Kinetics of Two Step Solar Thermochemical H_2O and CO_2 Splitting with CeO_2", D. Arifin, A.H. McDaniel, and A.W. Weimer, ASME 7th International Conference on Energy Sustainability, Minneapolis, MN, USA, 14-19 July, 2013.

"Advancing Oxide Materials for Thermochemical Production of Solar Fuels", J.E. Miller, A. Ambrosini, E.N. Coker, M.D. Allendorf, and A.H. McDaniel, *Energy Procedia,* 19th SolarPACES oral presentation and proceedings paper, Las Vegas, NV, USA 17-20 September, 2013.

"Annual Average Efficiency of a Solar Thermochemical Reactor", I. Ermanoski and N.P. Siegel, *Energy Procedia*, 19th SolarPACES poster presentation and proceedings paper, Las Vegas, NV, USA 17-20 September, 2013.

"Nonstoichiometric Perovskite Oxides for Solar Thermochemical H_2 and CO Production", A.H. McDaniel, A. Ambrosini, E.N. Coker, J.E. Miller, W.C. Chueh, R. O'Hayre, and J. Tong, *Energy Procedia*,19th SolarPACES oral presentation and proceedings paper, Las Vegas, NV, USA 17-20 September, 2013.

"Considerations in the Design of Materials for Solar-Driven Fuel Production Using Metal-Oxide Thermochemical Cycles", J. E. Miller, A. H. McDaniel, M. D. Allendorf, *Adv. Energy Mater.* accepted for publication 2013, doi:10.1002/aenm.201300469.

SUBTASK 1.2: ALD ACTIVE THIN FILMS/SUPPORT MATERIALS FOR FERRITE/HERCYNITE THERMOCHEMICAL REDOX CYCLE/SOLAR REACTOR

OBJECTIVE

The overall objective of this subtask is to continue with the encouraging investigation of active ferrite thin films prepared by atomic layer deposition (ALD) for the splitting of water via a solar thermochemical hercynite redox cycle. A key aspect is the in-situ preparation of an active ultra-thin and highly porous, large-pore-size reactive alumina substrate prepared by ALD using a polymer template. The ferrite reacts with alumina providing stable hercynite which has been demonstrated to form a reduced intermediate at temperatures ~ 150 ºC below that of conventional ferrites. Thin films of active materials reduce diffusion and thermal resistances. Investigation includes the formation of the substrate, deposition of active ferrite films, the isothermal cycling of the films under a controlled environment, an improved understanding of the underlying materials thermodynamics and kinetics, efficiency of the solar reactor and an on-sun demonstration of a single-tube isothermal solar redox reactor.

HERCYNITE REDOX NANOSTRUCTURED MATERIALS AND ISOTHERMAL CYCLING

Point of contact: Alan W. Weimer

PROJECT STATUS

Hercynite Materials and Isothermal Water-Splitting

This quarter focused on the isothermal cycling of "hercynite" materials over a wider range of temperatures and partial pressures of CO_2 than were previously investigated. Due to experimental complications regarding steam flow and condensation at high pressures, CO_2 splitting cycles were studied in place of water splitting cycles. The relative behavior and material productivity with respect to CO_2 splitting is comparable to that of water splitting and therefore overall observations made throughout the course of these experiments are translatable to water splitting and contribute to furthering understanding of isothermal cycling as a whole.

Experiments were run at a total pressure of 760 torr in an idealized stagnation flow reactor (SFR) at Sandia National Laboratories. Approximately 150 mg of sample material was placed in the SFR in a loosely packed manner to ensure that all surfaces were exposed to gases in the stagnation flow environment. An experimental matrix, shown in Figure 11, was generated based on a factorial design in order to efficiently probe a wide range of potential temperature and CO_2 partial pressure operating conditions. The experimental matrix spanned a temperature range from 1280°C to 1420°C and spanned a partial pressure of CO_2 range from 310 torr to 576 torr.

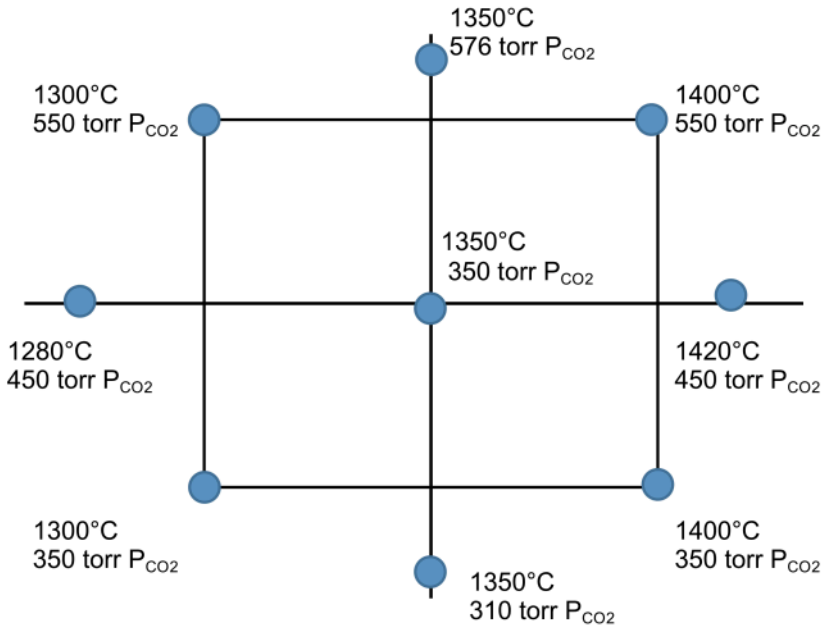

Figure 11. Design of experiments matrix for Isothermal CO_2 splitting runs with varying temperature and partial pressure of CO_2 conditions

An example of the raw signal measured during the CO_2 generation step (oxidation step) is shown in Figure 12. Specifically, Figure 12 shows the CO and O_2 evolution during oxidation of hercynite at 1400°C and 350 torr CO_2 partial pressure operating conditions.

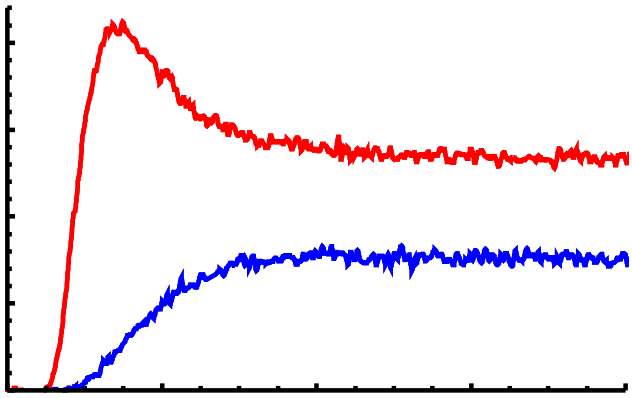

Figure 12. CO (red) and O_2 (blue) generation from oxidation of hercynite at 1400°C and 350 torr P_{CO2}.

The existence of an O_2 curve and CO shoulder exists due to catalytic CO_2 splitting which occurs along the inside of the reactor walls at these high temperatures. In order to correct for this

material-independent splitting, blanks were run at each of the conditions in the experimental matrix. The blank runs were conducted at identical reactor conditions in the absence of the hercynite material. The CO curves generated during blank runs were subtracted from the overall signal as shown in Figure 13 providing corrected CO curves.

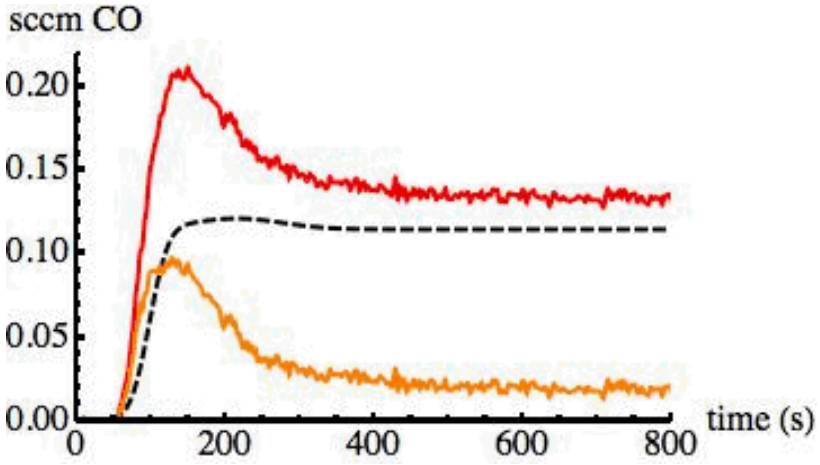

Figure 13. Uncorrected CO generation curve (red), blank CO generation curve (black), and corrected CO generation curve (orange).

It is important to note that the CO production curves are analyzed with respect to the total hercynite material mass. A close analysis of the hercynite material is underway in order to determine the percent of active material contained within the sample, however, corrections based on this percent active material are not reported here.

Corrected CO production curves were generated for each of the specified conditions in the experimental matrix. It was observed that the relative amount of CO generated increased with an increase in temperature and partial pressure of CO_2 in the reactor. An example of the increased peak CO production rate and generated CO (by inspection) with increasing temperature can be seen by the CO production curves during isothermal CO_2 splitting at temperatures of 1280°C, 1350°C, and 1420°C in 450 torr P_{CO2} as can be seen in Figure 14, Figure 15, and Figure 16 respectively.

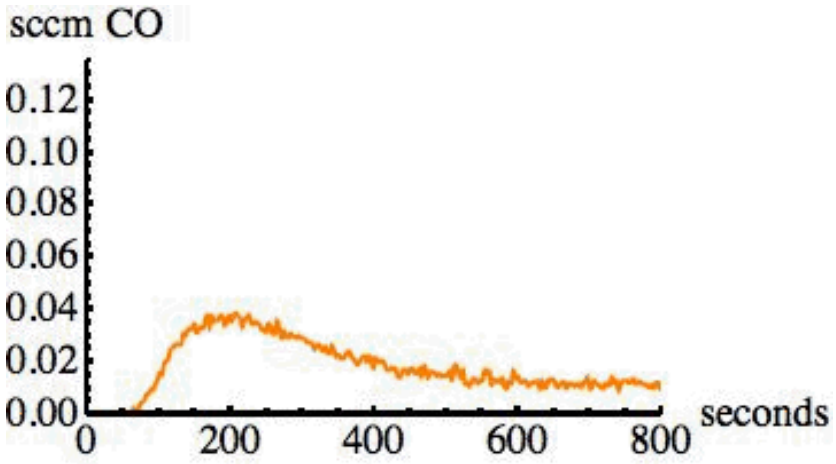

Figure 14. Corrected CO generation curve at 1280°C and 450 torr P_{CO2}.

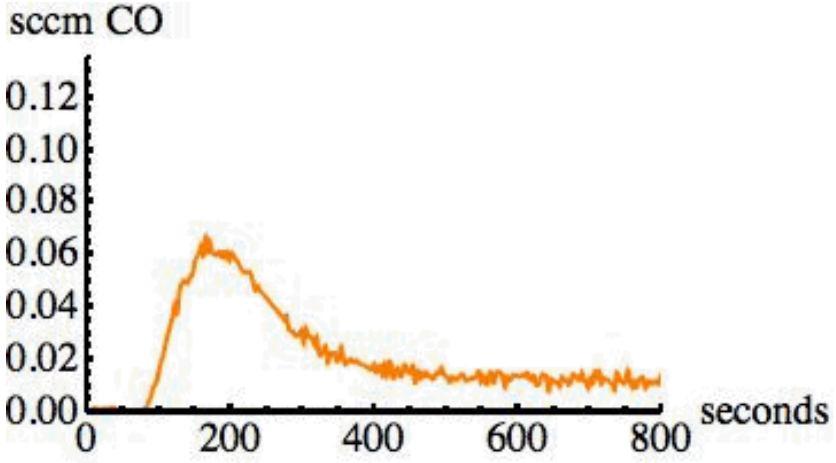

Figure 15. Corrected CO generation curve at 1350°C and 450 torr P_{CO2}.

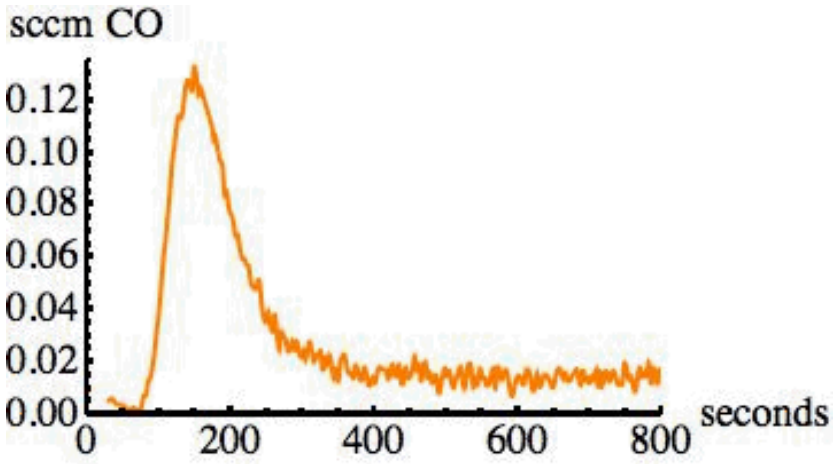

Figure 16. Corrected CO generation curve at 1420°C and 450 torr P_{CO2}.

There is a noticeable increase in total CO generated and in maximum CO sccm as the temperature increases. These results agree with the previously reported understanding that the productivity of the hercynite material benefits from high oxidation temperatures. Similar results were found with respect to an increase in P_{CO2} at constant reaction temperatures.

PLANS FOR NEXT QUARTER AND KEY ISSUES

With the experimental matrix completed in terms of gathering experimental data, the next quarter will focus on analyzing these curves to determine the kinetics governing the CO_2 oxidation of hercynite. A large complication in carrying out this analysis arises from the need to correct the CO production for the oxygen generated during the oxidation reactions. Due to upstream catalytic CO_2 splitting that occurs at the reactor walls, the material is exposed to a gaseous mixture of CO_2, CO, and O_2 during oxidation. Feeding O_2 in this manner causes the material uptake of the O_2, which results in a delay, Δt, in appearance of the O_2 generation curve when hercynite material is present as compared to the blank reactor O_2. This delay results in the inability to directly subtract the blank O_2 signal from the overall signal in order to determine the corrected O_2 curve. Accurately corrected O_2 and CO curves are needed to further conduct total CO generation and kinetic rate analysis. Therefore the next quarter will focus on 1) developing a meaningful O_2 analysis method that works around this complication and 2) developing a method by which to analyze the kinetics and define meaningful rate expressions of the hercynite oxidation reaction.

MULTI-TUBE SOLAR RECEIVER

Point of contact: Alan W. Weimer

Previous work described a 3D dynamic computational model coupling radiative transfer with fluid flow, heat transfer, mass transfer, and chemical reaction kinetics that was developed to evaluate the performance of the solar receiver. The solar receiver consists of an array of tubular

absorbers filled with the active material and contained within an insulated absorbing cylindrical outer cavity with a small aperture. Recent efforts have focused on comparing receiver behavior between temperature swing (TS) and isothermal (IT) configurations.

PROJECT STATUS

Multi-Tube Solar Receiver Modeling

Both TS and IT operation are evaluated with equivalent reduction and oxidation cycle times. Thus at any instant in time, pure argon is fed to half of the tubes, while pure steam is fed to the remaining tubes. The distinction between TS and IT operation in this work is made via the time dependence and directionality of the solar input. For TS operation, the solar input is directed at an angle toward one side of the receiver and switched to the opposing side after a pre-defined cycle time. For IT operation the solar input remains directed perpendicular to the aperture such that all tubes are illuminated during both reduction and oxidation, and the distinction between reduction and oxidation tubes is controlled purely by the inlet flow conditions. Spatial temperature variations between tubes are unavoidable and in the current work the term "isothermal" refers to temperatures which remain essentially uniform through time at any given position in the receiver.

Initial receiver dimensions were selected to produce the desired temperature range with a solar input of 4 kW. The cavity encloses six 2.62cm outer-diameter (2.3cm inner-diameter), 0.22m long flow tubes arranged on an arc angle adjacent to the back cavity wall. The cavity radius is the smallest possible to contain the tube array with a minimal wall clearance of 2cm. Initial tube arc angles were 240° and 180° for TS and IT configurations, leading to cavity sizes of 13.3cm and 16.2cm, respectively. The arc angle for the IT configuration was reduced relative to that for the TS configuration in order to promote uniform solar absorption between tubes.

The definition of solar-to-chemical receiver efficiency was updated from previous work and shown in equations 2-6. The total thermal input to the process is taken to be the sum of the solar energy incident on the exterior window surface, energy required to separate oxygen produced during the reduction from the inert, and the net energy necessary to vaporize the inlet steam and heat the inlet streams from ambient temperature to the inlet temperature in the CFD model after heat recuperation from the exit gas streams with assumed effectiveness ε_{gas}.

$$\overline{\eta} = \frac{\int_{cycle} \dot{n}_{H_2} LHV_{H_2} dt}{Q_{tot}} \tag{2}$$

$$Q_{tot} = \int_{cycle} \left(\dot{Q}_{solar} + \eta_{s-e} e_{O_2} \dot{n}_{O_2} \right) dt + Q_{gas,net} \tag{3}$$

$$Q_{gas,net} = \int_{cycle} \left(\dot{Q}_{in} - \varepsilon_{gas} \dot{Q}_{out} \right) dt \tag{4}$$

$$\dot{Q}_{in} = \dot{n}_{H_2O,in}\Delta H_{vap} + \int_{T_0}^{T_{in,ox}} \dot{n}_{H_2O,in}\hat{C}_{p,H_2O}dT + \int_{T_0}^{T_{in,red}} \dot{n}_{Ar}\hat{C}_{p,Ar}dT \quad (5)$$

$$\dot{Q}_{out} = \dot{n}_{H_2O,out}\Delta H_{vap} + \int_{T_0}^{T_{out,ox}} \left(\dot{n}_{H_2O,out}\hat{C}_{p,H_2O} + \dot{n}_{H_2}\hat{C}_{p,H_2}\right)dT + \int_{T_0}^{T_{out,red}} \left(\dot{n}_{Ar}\hat{C}_{p,Ar} + \dot{n}_{O_2}\hat{C}_{p,O_2}\right)dT \quad (6)$$

Calculations in this work were typically carried out with a cold inlet temperature such that the majority of the sensible enthalpy was provided by the solar input. Thus the net energy required to heat the inlet streams and vaporize steam ($Q_{gas,net}$) was restricted to a minimum value of zero in the event that the latent and sensible energy contained in the product streams exceeded that required to heat the inlet streams to the stipulated receiver inlet temperature. All pumping energy is neglected for the laboratory scale receiver considered in this study. The energy necessary for O_2 separation is included in equation (2) on an equivalent solar basis with an assumed solar-to-electric efficiency of 18%.

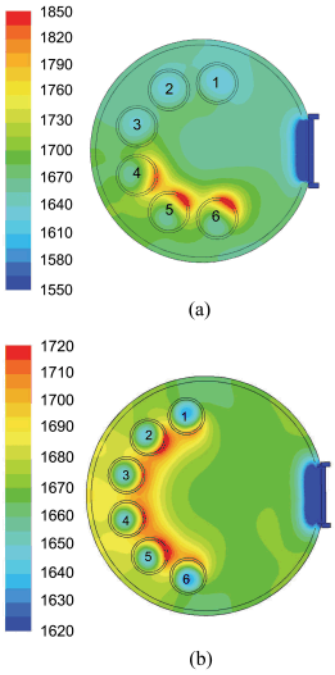

Figure 17. Temperature profiles (K) for (a) TS and (b) IT configurations.

Solar receiver cross-sections and calculated temperature profiles are depicted schematically in Figure 17 for temperature swing and isothermal cross-sections. Figure 18 illustrates the transient behavior of the maximum and volumetrically averaged temperatures attained on each of the two halves of the receiver along with corresponding H_2 and O_2 production rates. Maximum / volumetric averaged temperatures for the TS configuration are 1862K / 1620K for the reduction tubes and 1704K / 1585K for the oxidation tubes, respectively, though the highest temperatures in the reduction tubes are located in only a small fraction of the reactive material. Radiative

exchange between tubes and the cavity wall produces elevated temperatures in the oxidation tubes despite minimal direct solar absorption. For the IT configuration, maximum temperatures are essentially indistinguishable between tubes on opposing sides of the receiver, though volumetrically averaged temperatures oscillate with reduction/oxidation cycles. Maximum temperatures are 1716K, nearly 150K lower than the maximum reduction temperature in the TS configuration. Volumetrically averaged temperatures are similar for both TS and IT configurations.

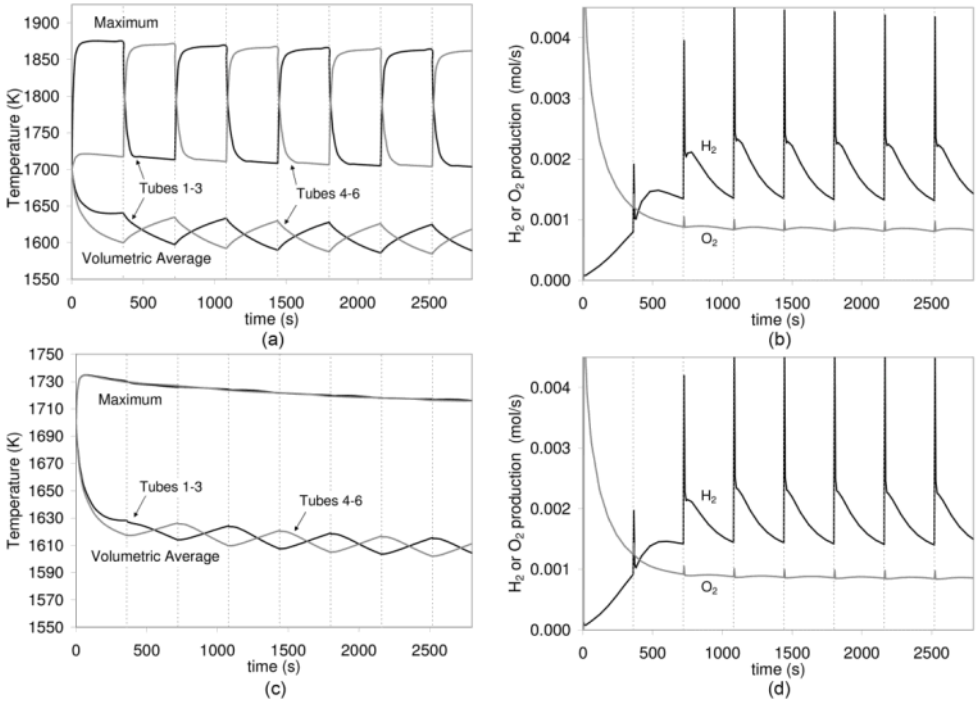

Figure 18. Computed maximum or volumetrically averaged temperatures and H_2, O_2 exit flow rates for (a, c) temperature swing and (b, d) isothermal configurations.

H_2 production occurs exclusively in the oxidation tubes, with the exception of the first few seconds of each cycle during which the H_2 produced during the previous oxidation cycle continues to exit the new reduction tubes. Currently employed rate expressions and equilibrium constants do not account for the possibility of competition between reduction and oxidation reactions, and thus O_2 production in the oxidation tubes is mathematically possible, provided temperatures are sufficiently high to favor thermal reduction. H_2 and O_2 production rates are remarkably similar for the TS and IT configurations, likely owing to the similarity in volumetrically averaged tube temperatures. Time-averaged H_2 production rates from the last cycle shown in Figure 18 from the IT configuration (0.00180 mol/s) are marginally higher than those from the TS configuration (0.00176 mol/s). Figure 18 reveals that large temperature swings between reduction and oxidation tubes may be difficult to achieve in a single reaction vessel with minimal conductive losses, as radiative exchange between the surfaces within the vessel serve to even out the temperature differences despite highly non-uniform solar absorption. Thus the

simulated TS configuration behaves quite similarly to the IT configuration with the exception of a small region of elevated temperature achieved on the front face of each reduction tube. Temperature separation in the TS configuration could potentially be improved by increasing the physical separation of reduction and oxidation tubes or allowing heat losses through the cavity wall; though an increase in H_2 production would need to be sufficient to offset the resultant increase in thermal loss.

The fractional time-averaged solar-to-chemical efficiency for the TS design above is calculated to be 8.8% for any gas-phase heat recuperation effectiveness above 42%. Without any gas-phase heat recuperation the efficiency drops slightly to 8.4% whereas neglecting energy necessary for O_2 separation raises the efficiency to 10.7%. The IT configuration performs similarly with a predicted solar to chemical efficiency of 9.0%. The calculated efficiency has little dependence on gas-phase heat recuperation effectiveness as the inlet temperatures are specified at 300K and thus all sensible heating is carried out in the receiver using a portion of the 4kW solar input. Solar reflection losses and conduction losses at the quartz window account for 9.5% and 11% of the total solar energy incident on the aperture, respectively, for both TS and IT configurations. Loss by thermal emission is responsible for 59% or 57% of the total solar input in the TS and IT configurations, respectively.

Figure 19 and Figure 20 depict the temporal and radial variations in temperature across a slice of one reduction and one oxidation tube in the vertical center plane for the last cycle shown in Figure 18. The flow time corresponds to the time elapsed since the beginning of the cycle. The spatial length scaled is defined in a direction perpendicular to the aperture such that $x\text{-}x_0 = r_{tube}$ at the side of the tube closest to the aperture. At the end of the oxidation cycle (t = 0 in Figure 19a or t = 360 in Figure 19b), the radial temperature profiles in the TS configuration are roughly symmetric as the tube is heated predominantly by radiative exchange with the surrounding surfaces in the absence of direct solar absorption. More than 90% of the temperature rise at the front side of the tube occurs during the first 60s of the cycle. Temperature decrease at the front side of the oxidation tube occurs predominantly via thermal emission leading to a slight local maximum in the oxidation tube temperature at short times. The temperature at the back side of the tube remains essentially constant during the cycle as this region is shielded from direct solar incidence during both reduction and oxidation. Tube centerline temperatures are as much as 150K lower than that at the tube edge. However, contributions from the slightly exothermic oxidation reaction serve to reduce this temperature gradient in oxidation tubes.

Temperature variations for the IT configuration (Figure 20) are much smaller than those observed for the TS configuration with only a 60K radial variation and little difference between reduction and oxidation tubes. Similar to the TS configuration, temperatures drop slightly in the reduction tubes in the early stages in the cycle, prior to rising in the latter stages as O_2 production slows. Oxidation tubes exhibit the reverse of this behavior, rising during the early stages of the oxidation cycle prior to dropping in the latter stages as H_2 production slows. The isothermal configuration exhibits greater front/back temperature asymmetry during the latter stages of the oxidation reaction owing to direct solar absorption. The distinct difference in the magnitude of temperature oscillations between the TS (Figure 19) and IT (Figure 20) configurations illustrates a potential advantage of isothermal operation. Though spatial temperature gradients cannot be

eliminated in the IT configuration, component lifetimes are expected to be substantially longer when cyclically exposed to less extensive temporal variations.

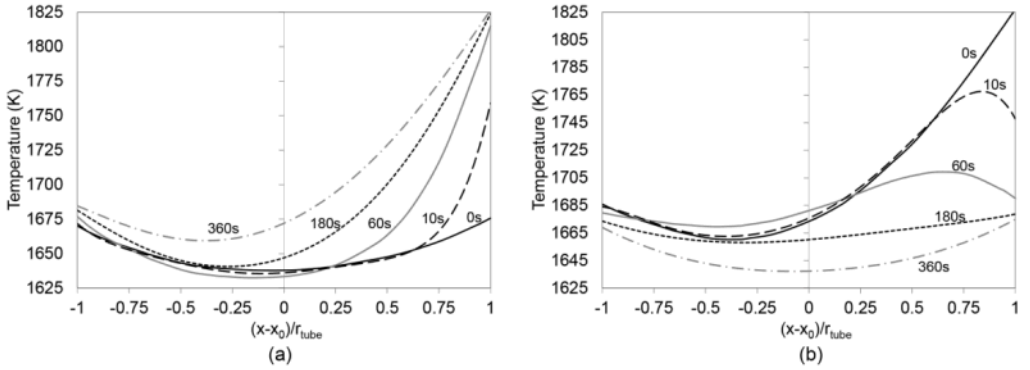

Figure 19. Radial temperature profiles in the TS configuration across (a) reduction tube 3 and (b) oxidation tube 4.

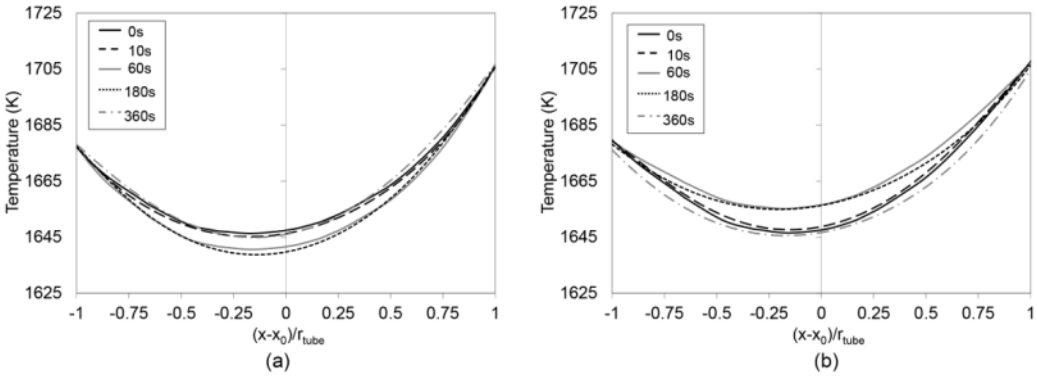

Figure 20. Radial temperature profiles in the IT configuration across (a) reduction tube 3 and (b) oxidation tube 4.

On-Sun Redox Demonstration

During this quarter, the research group utilized the National Renewable Energy Laboratory's (NREL) High Flux Solar Furnace (HFSF) in order to test the reduction/oxidation of hercynite materials on sun. The University of Colorado reactor allows for a multi tube configuration, with a quartz window port on the front.

For our testing on-sun, a single silicon carbide tube was used, in lieu of installing all five tubes. The tube was then filled with 1-mm inert alumina pellets up to the center of the tube in order to put the active material as close to the focal point of the secondary concentrator as possible. In order to prevent the active material from reacting with the silicon carbide containment tube, a

layer of inert zirconia felt was placed around the inner diameter of the containment tube to create a barrier.

Helium was used as the inert gas carrier for the reaction tube as well as the reflective cavity. The flow for the reaction tube was kept at 30 ml/min for the duration of the experiment. A Stanford Research System QMS 200 was used in order to identify hydrogen gas generation. The reactor (Figure 21) was heated using concentrated sunlight at a rate of 50 deg C/min, to 1350 °C. An attenuator was used to control the amount of concentrated sunlight that was entering the reactor, therefore controlling the heating rate. The tube temperature was read using a pyrometer. Once the tube temperature registered 1350 °C, a one hour hold began with inert flowing through the system. After the one hour purge was complete, steam was introduced using a syringe pump at a rate of 0.08 ml/min for 30 minutes. Once this step was completed, the cycle began over again, based on availability of sunlight.

Figure 21. Picture of reactor while testing on-sun at NREL

Due to some issues with weather not cooperating, and reconfiguring portions of the reactor that differed from previous experiments, the research team was able to only get one run with multiple cycling in before the reserved time at the HFSS was up. A path forward for subsequent experiments at NREL is discussed in the next section. The hydrogen gas generation signal as read from the mass spectrometer, showed that hydrogen gas was evolved during isothermal steam injection.

Going forward, the research group plans to use an alumina or zirconia tube in order to eliminate any reactivity issues between the materials. This would also remove the need for the zirconia felt that was required; however, the inert alumina spheres would remain in the tube in order to ensure proper placement of the active material. The only downside to using differing materials of tube is that they are more susceptible to thermal shock, and the ramp rate would need to be 20 deg C/min or less.

PLANS FOR NEXT QUARTER AND KEY ISSUES

Planned work to be carried out over the next quarter will involve further investigation of alternative tube configurations. The results described above indicate that receiver performance is controlled by a small number of parameters, particularly the active material cross-sectional area, aperture size, and number of tubes. This subset of parameters will be investigated in more detail via a response surface design to identify potential optima in efficiency. Similar sets of calculations will then be carried out for the isothermal design, thereby allowing detailed comparison of the performance between temperature swing and isothermal operation on the basis of an ideal receiver configuration for each design.

PUBLICATIONS/PRESENTATIONS

Muhich, C.L., B.W. Evanko, K.C. Weston, P. Lichty, X.H. Liang, J. Martinek, C.B. Musgrave, and A.W. Weimer, "Efficient Generation of H2 by Splitting Water with an Isothermal Redox Cycle," Science, 341, 540-542 (August 2, 2013).